

# Parallel 3D Finite Element Numerical Modelling of DC Electron Guns

E. Prudencio<sup>†</sup>, A. Candel, L. Ge, A. Kabel, K. Ko, L. Lee, Z. Li, C. Ng, G. Schussman

**Abstract**—In this paper we present Gun3P, a *parallel* 3D finite element application that the Advanced Computations Department at the Stanford Linear Accelerator Center is developing for the analysis of beam formation in DC guns and beam transport in klystrons. Gun3P is targeted specially to complex geometries that cannot be described by 2D models and cannot be easily handled by finite difference discretizations. Its parallel capability allows simulations with more accuracy and less processing time than packages currently available. We present simulation results for the L-band Sheet Beam Klystron DC gun, in which case Gun3P is able to reduce simulation time *from days to some hours*.

**Index Terms**—Electron guns, parallel computing, finite element method, electrostatics, magnetostatics, particle tracking.

## I. INTRODUCTION

THERE are many software packages available for the simulation of DC guns and collectors [1] [2] [3] [4], e.g. MICHELLE [5] [6], TRAK [7] and EGUN [8]. Currently available codes for modeling DC guns run on single CPU machines. The size of the problem and the amount of design details that can be modeled using these codes are limited by the memory and speed of a single processor. The Advanced Computations Department (ACD) at the Stanford Linear Accelerator Center (SLAC) is developing the Gun3P application, which overcomes these limitations by using high-order finite elements over *curved* tetrahedra and *parallel* processing for accuracy and speed.

The paper is organized as follows. In Section II we briefly describe Gun3P and its underlying algorithm. Section III presents L-band Sheet Beam Klystron (LSBK) DC gun simulation results obtained with Gun3P, followed by conclusions in Section IV. In the Appendix we focus on the numerical aspects of Gun3P, including the mathematical derivation of the discrete equations solved and some convergence studies.

## II. GUN3P OVERVIEW

The objective of Gun3P is to compute the equilibrium state of four physical observables present in DC gun operations (see Figure 1): the electrostatic field, the self-magnetostatic field and the charge and current densities related to a beam of charged particles. Its algorithm consists of a sequence of computing *cycles* until a convergence criterion is achieved, as shown in Figure 2. Each cycle groups three computational

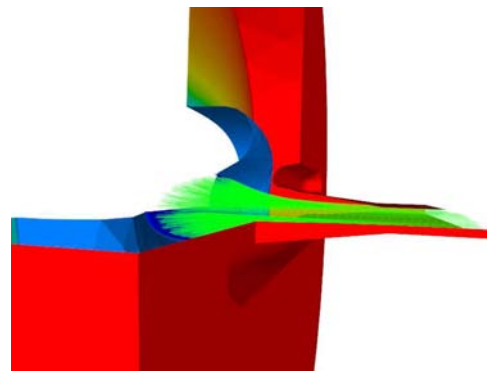


Fig. 1. Equilibrium electric potential and beam trajectory obtained with Gun3P. The picture shows three-fourths of the geometry so that the beam can be better visualized. The blue region corresponds to the cathode at 0V, the red surface corresponds to the anode at 115KV and the colorful curves correspond to the change of electric potential along the gap region between cathode and anode. The thin green lines model the beam travelling from the cathode towards the narrow exit gap on the right. The evaluation of the beam self-magnetic field is essential for simulation correctness.

tasks: electrostatic solver, magnetostatic solver and particle tracker. Parallel computing is used in all three tasks.

Gun3P extends the libraries already used for the Omega3P and Track3P codes [9] developed at ACD under the Scientific Discovery through Advanced Computing initiative (SciDAC [10]) of the Office of Science of the Department of Energy (DOE). It is written in C++, uses the MPI paradigm for parallel processing and runs on UNIX type operating systems. Postprocessing is done with v3d, the 3D visualization package developed by ACD under SciDAC as well.

Gun3P expresses the electrostatic field  $\mathbf{E}$  and the magnetostatic flux density  $\mathbf{B}$  in terms of scalar potential  $\phi$  and vector potential  $\mathbf{A}$ ,

$$\mathbf{E} = -\nabla\phi \quad \text{and} \quad \mathbf{B} = \nabla \times \mathbf{A},$$

so that the steady-state Maxwell equations  $\nabla \times \mathbf{E} = \mathbf{0}$  and  $\nabla \cdot \mathbf{B} = 0$  are automatically satisfied. At any given cycle, the electrostatic solver deals with the equation

$$-\nabla \cdot (\epsilon \nabla \phi) = \rho \quad (1)$$

and the magnetostatic solver deals with the equation

$$\nabla \times (\mu^{-1} \nabla \times \mathbf{A}) = \mathbf{J}, \quad (2)$$

where  $\epsilon$  is the permittivity,  $\mu$  is the permeability, and the charge density  $\rho$  and current density  $\mathbf{J}$  are computed from trajectories of the previous cycle (both terms are zero for the first cycle). We assume homogeneous isotropic media, so that  $\epsilon$  and  $\mu$

<sup>†</sup>Advanced Computations Department, Stanford Linear Accelerator Center, 2575 Sand Hill Road, MS 27, Menlo Park, CA 94025. Phone: 650-926-5389; fax: 650-926-4603; e-mail: prudenci@slac.stanford.edu. This work was supported by the U. S. Department of Energy under contract DE-AC02-76SF00515.

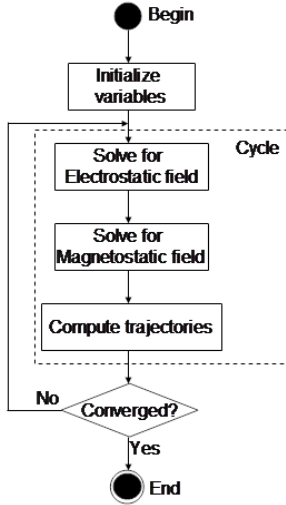


Fig. 2. Overview of Gun3P's algorithm.

are constant scalars. Proper boundary conditions on  $\phi$  and  $\mathbf{A}$ , detailed in the Appendix, are also imposed. Gun3P relies on the finite element method over *curved* tetrahedral meshes with geometric order  $q \leq 2$  for the discretization of both  $\phi$  and  $\mathbf{A}$ . Scalar basis functions up to order  $p_E = 4$  can be used for computing the discrete  $\phi$  and vector basis functions up to order  $p_B = 6$  can be used for computing the discrete  $\mathbf{A}$ .

Once the field potentials are computed, particles are emitted and tracked. Figure 3 presents the main parameters involved in the emission model. The emission positions are assigned during initialization and do not vary through cycles. Without loss of generality, we assume a grounded cathode. Let  $m_0$  and  $e$  indicate the particle rest mass and electric charge,  $\mathbf{x}_0$  indicate a emission position at the cathode and  $\hat{\mathbf{n}}$  indicate the outward unit normal at  $\mathbf{x}_0$ . Also, given a user-specified distance  $d$  (e.g.  $d = 100\mu\text{m}$ ) from the cathode, let  $\mathbf{x}_d = \mathbf{x}_0 - d\hat{\mathbf{n}}$ , let  $\phi_d$  and  $\mathbf{E}_d = -\nabla\phi_d$  indicate the electric potential and the electric field at  $\mathbf{x}_d$  and let  $v_d$  indicate the velocity magnitude satisfying

$$\frac{m_0 v_d^2}{2} = -e\phi_d.$$

Gun3P emits a particle at  $\mathbf{x}_0$  with constant velocity [7]

$$\mathbf{v}_0 = -\frac{2}{3}v_d\hat{\mathbf{n}}$$

and associates to it a current density  $J_{cathode}$  according to Child-Langmuir's law [11] [12] [13]

$$J_{cathode} = \frac{4}{9}\epsilon\sqrt{\frac{2|e|\phi_d^{3/2}}{m_0 d^2}}. \quad (3)$$

Once the particle reaches  $\mathbf{x}_d$ , its velocity is set to [7]

$$\mathbf{v}_d = v_d \frac{e\mathbf{E}_d}{\|e\mathbf{E}_d\|}$$

and its trajectory is computed through the relativistic Lorentz equation

$$m_0 \frac{d(\gamma\mathbf{v})}{dt} = e[\mathbf{E} + \mathbf{v} \times \mathbf{B}], \quad (4)$$

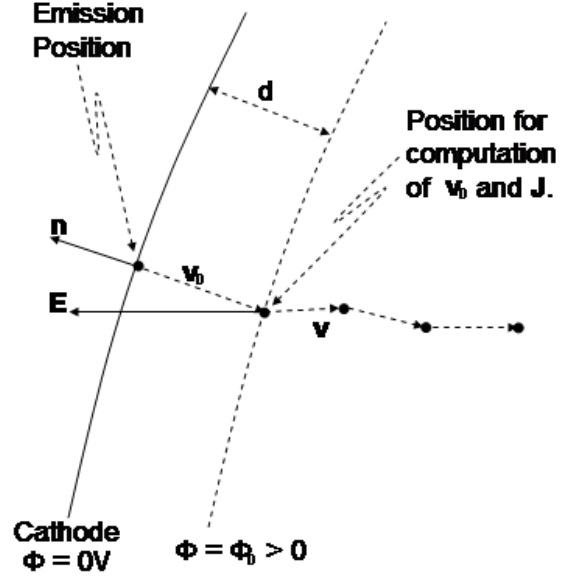


Fig. 3. Emission model currently used by Gun3P.

where  $\gamma$  is the relativistic mass factor. The Boris algorithm [14] is used for the discretization of (4). Currently Gun3P does not model any thermal effects at the cathode.

Once all particles are tracked, Gun3P loops to the next cycle, updating  $\rho$  and  $\mathbf{J}$  in (1) and (2). As the inter-cycle loop continues, one expects all computed values to stabilize, e.g. particle trajectories, field magnitudes and gun current. In fact, Gun3P loops until some convergence criterion is satisfied or the maximum user-defined number of cycles is achieved. Cycle convergence criteria are discussed in the Appendix.

Table I summarizes the main input parameters, while Table II shows some output parameters. The  $\epsilon_y$  emittance formula used by Gun3P is

$$\epsilon_y = 2\pi \sqrt{\langle y^2 \rangle \left\langle \frac{\dot{y}^2}{\dot{z}^2} \right\rangle - \left\langle y \frac{\dot{y}}{\dot{z}} \right\rangle^2}, \quad (5)$$

where the dot sign indicates the derivative with respect to the time variable and the averages are taken over to total number of particles. Formula (5) assumes symmetry w.r.t. to  $x \times z$  plane, that is,  $\langle y \rangle = 0$ ,  $\langle \dot{y}/\dot{z} \rangle = 0$  and  $\langle y\dot{y}/\dot{z} \rangle = 0$ . Similar formula and assumption are used for  $\epsilon_x$  emittance.

### III. LSBK DC GUN SIMULATION

The sheet beam klystron (SBK) is being developed at SLAC for the International Linear Collider as an alternative high power RF source to conventional pencil beam klystrons, offering advantages such as simpler fabrication and longer life expectation due to lighter cathode loading. Because of the elongated elliptical beam transverse profile, SBK simulations are fully three dimensional.

Starting with an LSBK CAD/CAM model [15], we first generate a mesh using the Cubit package [16]. Figure 4 shows four different mesh views obtained with ACD's v3d visualization package. The mesh is finer in and around the

TABLE I  
MAIN GUN3P INPUT PARAMETERS. LETTER “E,B,T” REFERS TO  
ELECTROSTATIC/MAGNETOSTATIC/TRACKING PROBLEM.

Problem	Symbol	Meaning
All	# cycles	Number of cycles
	# elems	Number of tetrahedra
	$q$	Geometric order
	# cpus	Total number of cpus used
E	$V_{focus}$	Electric potential at focus electrode
	$V_{anode}$	Electric potential at anode
	$p_E$	Order of basis functions
B	$p_B$	Order of basis functions
T	$d$	Distance from cathode where Child-Langmuir’s law is applied
	N	Total number of particles
	$\Delta t$	Time step

TABLE II  
SOME OUTPUT PARAMETERS. “DOF” MEANS “DEGRESS OF FREEDOMN”.

Symbol	Meaning
$I$	Gun current
$J_{cathode}$	Current density profile at cathode
$\epsilon_y$	Emittance $y$ at a cross plane
$\rho$	Charge density profile at a cross plane
Hitting percentage	Percentage of particles hitting anode
# dof <sub>E</sub>	Number of dof for electrostatic problem
# dof <sub>B</sub>	Number of dof for magnetostatic problem
# time steps/cycle	Number of time steps per cycle
Run time	Run time

region of particle trajectories. In the simulations presented here, the forward direction is parallel to the  $z$  axis.

We then run Gun3P with the input parameters given in Table III and obtain the results shown in Table IV. MICHELLE [15] results, obtained with one processor, are shown for benchmarking purposes. The comparison in Table IV highlights the advantage of using parallel computing in Gun3P, namely the reduction of run time *from days to hours*.

Figure 5 shows the equilibrium particle trajectories. The beam width in the  $x$ -direction is practically constant throughout the whole path from cathode to the exit gap.

Gun3P also monitors a variety of beam features. Figure 6, for instance, shows phase-spaces on three cross  $x \times y$  planes positioned along the  $z$  axis. The beam leaves the cathode undergoing strong focusing (Figures 5-(a) and 6-(a)), travels parallel to the  $z$  axis around  $z = 14$ cm, the region of beam waist (Figure 6-(b)), and shows some expansion at  $z = 18$ cm, the exit gap region (Figure 6-(c)).

Figure 7 shows the  $\epsilon_y$  emittance profile along the  $z$  axis, sharply decreasing near the cathode, since that is the region where the beam experiments the strongest acceleration in the forward direction.

In both Figures 6 and 7 we show results for four different meshes, from the coarsest with 479k tetrahedra to the finest with 1,817k tetrahedra. The results change less as the mesh is refined, a necessary condition for correctly discretized

TABLE III  
INPUT VALUES USED FOR GUN3P AND MICHELLE SIMULATIONS.

Problem	Input Parameter	Gun3P Value	MICHELLE Value
All	# cycles	41	80
	# elems	1,316,530 tetrahedra	1,073,000 hexahedrons
	$q$	2	1
	# cpus	48 (1.9 GHz each)	1 (3.0 GHz)
E	$V_{focus}$ (V)	-500	-500
	$V_{anode}$ (V)	115,000	115,000
	$p_E$	3	1
B	$p_B$	1	unknown
T	$d$ ( $\mu$ m)	100	unknown
	N	145,675	96,064
	$\Delta t$ (ps)	2	unknown

TABLE IV  
OUTPUT VALUES OBTAINED BY GUN3P AND MICHELLE SIMULATIONS.

Output parameter	Gun3P Value	MICHELLE Value
$I$ (A)	129.3	129.3
$J_{cathode}$ (A/cm <sup>2</sup> )	min = 1.7528 max = 2.3622	min = 1.7500 max = 2.4000
$\epsilon_{y,z=18cm}$ ( $\pi$ mm-mrad)	4.3	unknown
$\rho_{z=14cm}$ (mC/m <sup>3</sup> )	max = 3.9	unknown
Hitting percentage	0%	0%
# dof <sub>E</sub>	6,114,694	unknown
# dof <sub>B</sub>	1,599,393	unknown
# time steps/cycle	785	unknown
Run time (hrs)	5.5	63.6

problems.

In Figures 8 and 9 we again compare some Gun3P results to MICHELLE ones. Figure 8 shows the current density profile at the cathode and Figure 9 shows the charge density profile on the cross plane at  $z = 14$ cm.

Results in Figures 8-(a) and 8-(b) agree pretty well. Each dot in Figure 8-(a) represents a Gun3P particle and the color varies according to the current density computed with Child-Langmuir’s emission law (3). The appearance of Figure 8-(a) is smooth. Indeed, since Gun3P uses tetrahedral meshes, particles are distributed “everywhere”, not just at regular positions inside cells of regular meshes. The distribution of emission positions over *sufficiently fine* irregular meshes contributes to more realistic beam simulations.

Figure 9-(a) is obtained by dividing the cross section into a rectangular grid of cells and adding the contributions of all particles crossing each cell, as explained in the Appendix.

In Figure 10 we analyze the same cross section of Figure 9 but now plot a dot for each particle and color the dots according to the current density of the particle *at the cathode* (Figure 8). With this approach we are able to indicate which cathode region a particle in Figure 10 came from. The fact that color profile in the vertical direction is preserved, from the cathode at around  $z = 0$ cm to the cross section at  $z = 14$ cm is consistent with a laminar flow.

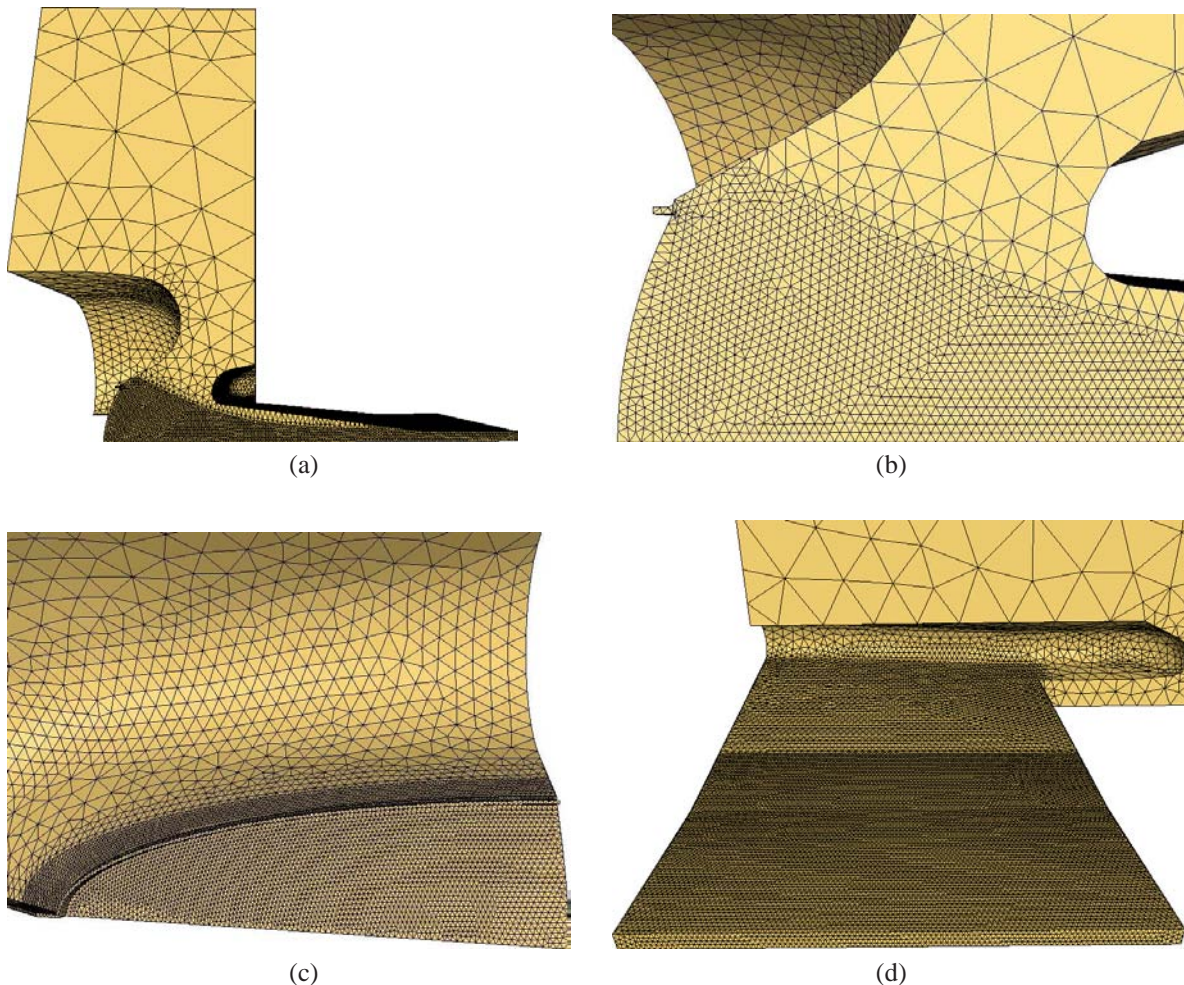


Fig. 4. A mesh for one-fourth of LSBK gun: (a)  $y \times z$  view, with the hidden horizontal symmetry plane being  $x \times z$ , the bottom horizontal line corresponding to the  $z$  axis and the right-bottom point being  $(x, y, z) = (0, 0, 18\text{cm})$ ; (b) zoom of figure (a), with the left-bottom point being  $(x, y, z) = (0, 0, 0)$ ; (c)  $x \times y$  view highlighting the cathode, part of the focus electrode and the gap between them; (d)  $x \times y$  view highlighting the anode and the exit gap.

Gun3P users can also visualize computed fields as *cones*, as well as their magnitudes at boundary surfaces and cross planes, as in Figure 11.

In Figure 12 we show Gun3P scalability. Although the real scalability curve is always expected to diverge from the ideal scalability line, there is room for improvement through the use of better linear preconditioners for the electrostatic and magnetostatic discrete systems of equations.

#### IV. CONCLUSIONS

The *parallel* 3D finite element Gun3P code was used for the simulation of LSBK DC gun and showed very good agreement to MICHELLE on gun current and current density profile at the cathode. Besides having parallel capabilities, Gun3P is able to calculate and generate a variety of parameters, profiles, images and movies through detailed built-in monitoring of particle trajectories and fields. Some examples of output data include gun current, charge and current densities, phase-spaces, emittances, fields, beam path and beam cross shape.

Possible modelling improvements are the inclusion of thermal noise into particle emission and curvature effects into

Child-Langmuir's law. Possible numerical enhancements are the use of meshes that are finer in the focusing direction ( $y$  axis in this paper), for the calculation of less noisy phase-spaces and beam cross shapes, and the use of better linear solvers on the electrostatic and magnetostatic problems, for the improvement of Gun3P performance and scalability.

The purpose of any simulation package is to provide its users (engineers and scientists) details on all possible features of the device being designed or studied. The combination of parallel computing with conformal grids and high-order basis functions positions Gun3P as a competitive package for the design of modern DC gun devices with precise simulations under reasonable run times of *hours, instead of days*.

#### ACKNOWLEDGMENTS

The authors would like to thank Alexander Burke from the Klystron Department at SLAC for providing LSBK model files and MICHELLE results. We also acknowledge the contributions from our SciDAC collaborators in numerous areas of computational science. This research was supported by the U. S. DOE under contract DE-AC02-76SF00515, and

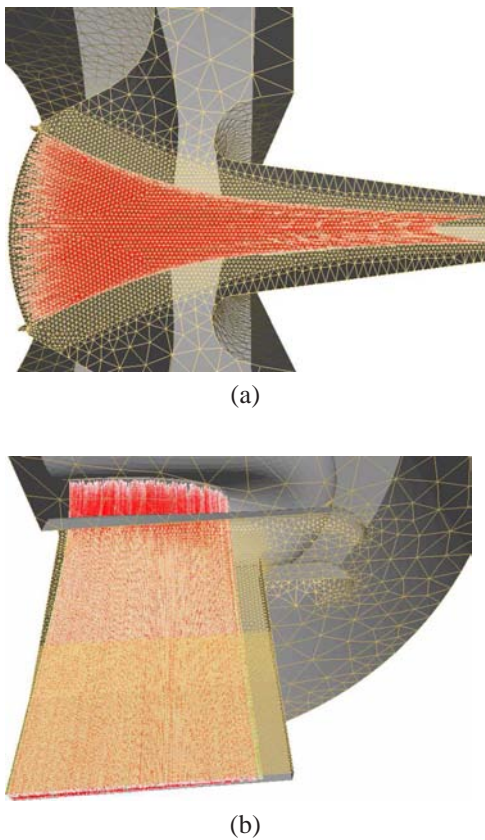


Fig. 5. Different views of the same particle trajectories.

used resources of the National Energy Research Scientific Computing Center under contract DE-AC03-76SF00098 of the Office of Science of the U. S. DOE.

REFERENCES

- [1] P. T. Kirstein, G. S. Kino, and W. E. Waters, *Space-Charge Flow*. McGraw-Hill Book Company, 1967.
- [2] S. Humphries Jr., *Principles of Charged Particle Acceleration*. John Wiley & Sons, 1986.
- [3] —, *Charged Particle Beams*. John Wiley & Sons, 1990.
- [4] Jon C. Freeman, “Preliminary Study of Electron Emission for Use in the PIC Portion of MAFIA,” NASA/TM-2001-210890, 2001.
- [5] J. Petillo et al., “The MICHELLE Three-Dimensional Electron Gun and Collector Modeling Tool: Theory and Design,” *IEEE Trans. Plasma Sc.*, vol. 30, no. 3, pp. 1238–1264, 2002.
- [6] E. M. Nelson and J. J. Petillo, “Current accumulation for a self magnetic field calculation in a finite-element gun code,” *IEEE Trans. Magn.*, vol. 41, no. 8, pp. 2355–2361, 2005.
- [7] S. Humphries Jr., “Numerical modeling of space-charge-limited charged-particle Emission on a conformal triangular mesh,” *Journal of Computational Physics*, vol. 125, pp. 488–497, 1996.
- [8] W. B. Herrmannsfeldt, “EGUN: An Electron Optics and Gun Design Program,” Stanford Linear Accelerator Center, Publication SLAC-231, 1988.
- [9] DOE Office of Science, “Scientific discovery through advanced computing,” <http://www.scidac.gov>, 2001–2007.
- [10] K. Ko et al., “SciDAC and the International Collider: Petascale Computing for Terascale Accelerator,” *SciDAC 2006 Conference*, Denver, CO, June 25–29, 2006.
- [11] I. Langmuir, “The effect of space charge and initial velocities on the potential distribution and thermionic current between parallel plate electrodes,” *Phys. Rev.*, vol. 21, pp. 419–435, 1923.
- [12] I. Langmuir and K. B. Blodgett, “Currents limited by space charge between coaxial cylinders,” *Phys. Rev.*, vol. 22, pp. 347–357, 1923.

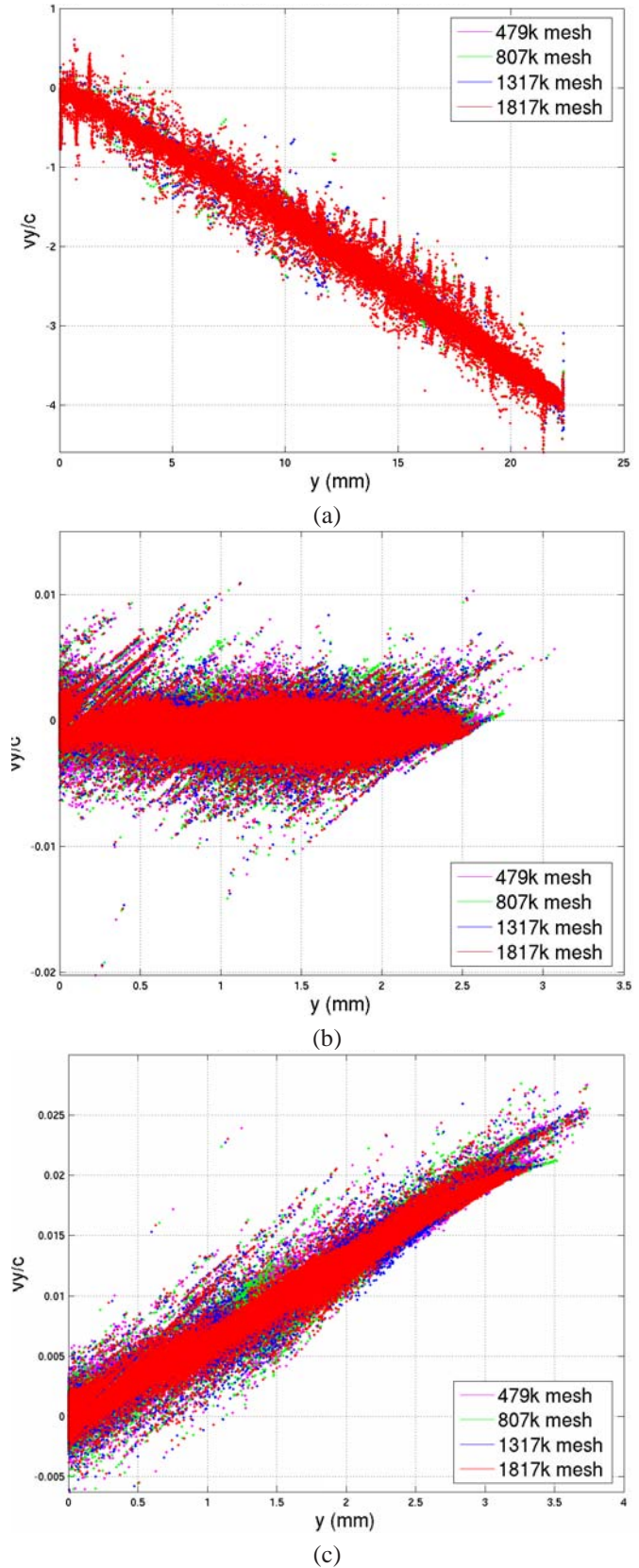


Fig. 6. Evolution of  $y - v_y$  phase-space along  $z$  axis. (a) at cathode; (b) at  $z = 14\text{cm}$  (beam waist region); (c) at  $z = 18\text{cm}$  (exit gap).

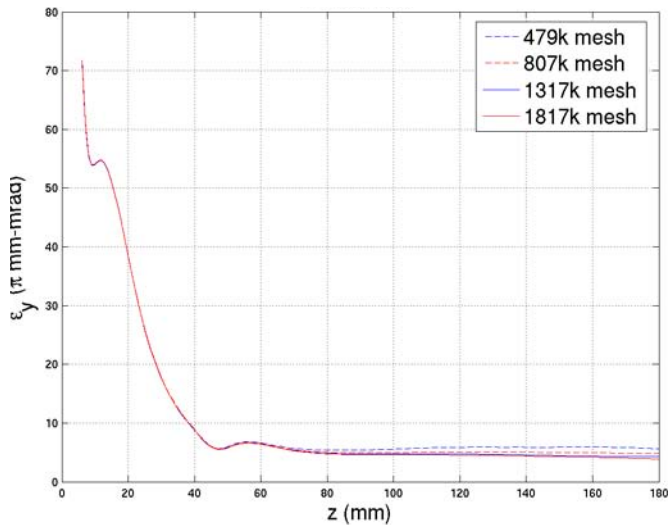


Fig. 7. Emittance  $\epsilon_y$  along  $z$  axis, according to formula (5).

- [13] —, “Currents limited by space charge between concentric spheres,” *Phys. Rev.*, vol. 24, pp. 49–59, 1924.
- [14] C. K. Birdsall and A. B. Langdon, *Plasma Physics via Computer Simulation*. McGraw-Hill Book Company, 1985.
- [15] Alexander Burke, internal communications, SLAC, 2007.
- [16] Sandia Corporation, “Cubit geometry and mesh generation toolkit,” <http://cubit.sandia.gov>, 1995–2007.
- [17] M. L. Barton and Z. J. Cendes, “New vector finite elements for three-dimensional magnetic field computation,” *J. Appl. Phys.*, vol. 61, no. 8, pp. 3919–3921, 1987.
- [18] J. Jin, *The Finite Element Method in Electromagnetics*. John Wiley & Sons, 1993.
- [19] P. G. Ciarlet, *The Finite Element Method for Elliptic Problems*. North-Holland Publishing Company, 1978.
- [20] J. P. Webb and B. Forghani, “Hierarchical Scalar and Vector Tetrahedra,” *IEEE Trans. Magn.*, vol. 29, no. 2, pp. 1495–1498, 1993.
- [21] J. P. Webb, “Hierarchical Vector Basis Functions of Arbitrary Order for Triangular and Tetrahedral Finite Elements,” *IEEE Trans. Ant. Prop.*, vol. 47, no. 8, pp. 1244–1253, 1999.
- [22] J.-F. Lee, D. K. Sun, and Z. J. Cendes, “Tangential Vector Finite Elements for Electromagnetic Field Computation,” *IEEE Trans. Magn.*, vol. 27, no. 5, pp. 4032–4035, 1991.
- [23] A. Ahagon and T. Kashimoto, “Three-dimensional Electromagnetic wave analysis using high order Edge Elements,” *IEEE Trans. Magn.*, vol. 31, no. 3, pp. 1753–1756, 1995.
- [24] A. Bossavit, “A Rationale for ‘Edge-Elements’ in 3-D Fields Computations,” *IEEE Trans. Magn.*, vol. 24, no. 1, pp. 74–79, 1988.
- [25] D.-K. Sun, J.-F. Lee, and Z. Cendes, “Constructions of Nearly Orthogonal Nedgelec Bases for Rapid Convergence with Multilevel Preconditioned Solvers,” *SIAM J. Sci. Comput.*, vol. 23, no. 4, pp. 1053–1076, 2001.
- [26] J. P. Webb, “Edge Elements and What They Can do for You,” *IEEE Trans. Magn.*, vol. 29, no. 2, pp. 1460–1465, 1993.
- [27] D. Sun, J. Manges, and X. Yuan, “Spurious modes in finite-element methods,” *IEEE Ant. Propag. Magn.*, vol. 37, no. 5, pp. 12–24, 1995.
- [28] R. Albanese and G. Rubinacci, “Integral formulation for 3D eddy-current computation using edge elements,” *IEE Proceedings*, vol. 135A, no. 7, pp. 457–462, 1988.
- [29] —, “Magnetostatic field computations in terms of two-component vector potentials,” *Int. J. Num. Meth. Eng.*, vol. 29, pp. 515–532, 1990.
- [30] O. Bíró and K. Preis, “On the Use of the Magnetic Vector Potential in the Finite Element Analysis of Three-Dimensional Eddy Currents,” *IEEE Trans. Magn.*, vol. 25, no. 4, pp. 3145–3159, 1989.
- [31] N. A. Golias and T. D. Tsiboukis, “Magnetostatics with Edge Elements: A numerical investigation in the choice of the tree,” *IEEE Trans. Magn.*, vol. 30, no. 5, pp. 2877–2880, 1994.
- [32] Z. Ren, “Influence of the R.H.S. on the convergence behaviour of the curl-curl Equation,” *IEEE Trans. Magn.*, vol. 32, no. 3, pp. 655–658, 1996.

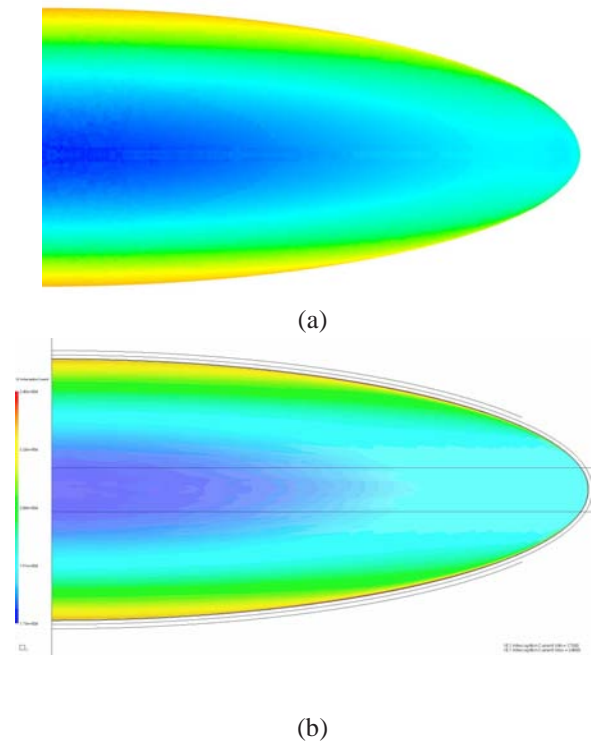


Fig. 8. Current density profile  $J$  ( $A/cm^2$ ) on the cathode, from minimum/blue value to maximum/red value: (a) Gun3P results; (b) MICHELLE results. In the case of Gun3P, each colorful dot corresponds to a particle. Minimum and maximum values are available in Table IV.

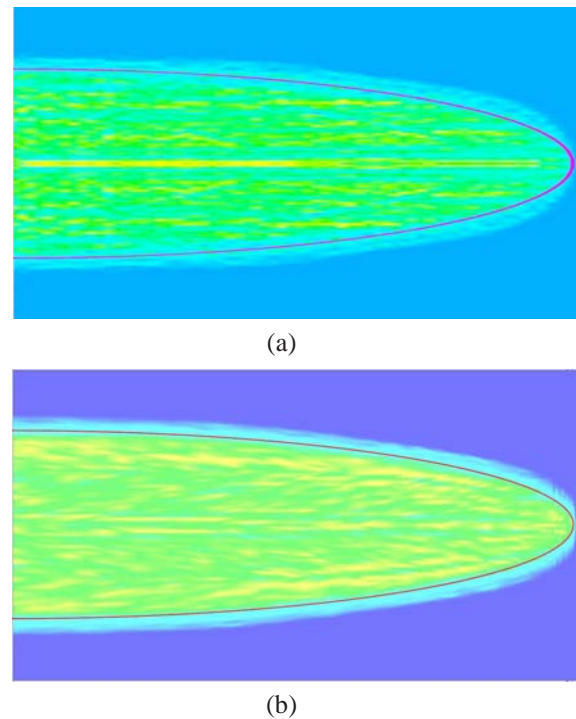


Fig. 9. Charge density profile  $\rho$  ( $mC/m^3$ ) on the rectangular cross section at  $z = 14cm$ , from minimum/blue value to maximum/yellow value: (a) Gun3P results; (b) MICHELLE results. For an easier comparison, both pictures show the same red ellipse with half-axes 2.25mm and 9.21cm.

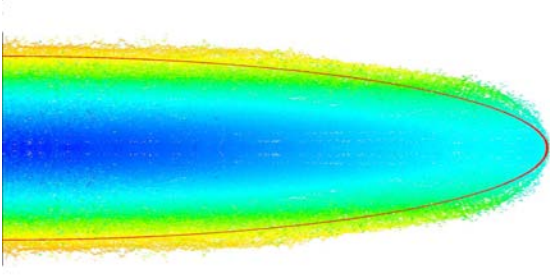


Fig. 10. Particle distribution at the rectangular cross section at  $z = 14\text{cm}$ , the same cross section of Figure 9. Each colorful dot corresponds to a particle and each particle is colored according to “its” current density at the cathode (see Figure 8-(a)). The red ellipse drawn in this picture has the same dimensions as in Figure 9.

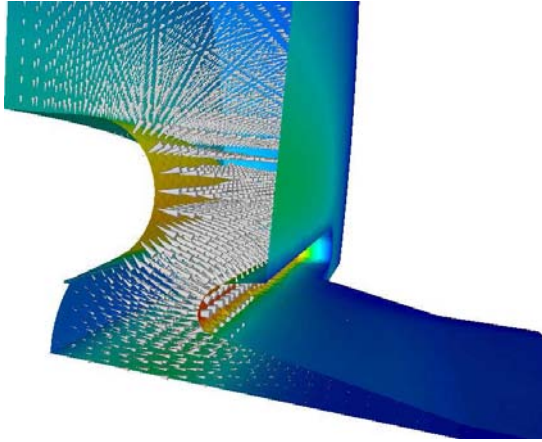


Fig. 11. Electrostatic field visualization. Cone directions indicate the field direction and the larger a cone is, the larger is the field magnitude at the corresponding location. The surface colors in this picture show the magnitude of the electric field, not the electric potential (shown in Figure 1, for instance).

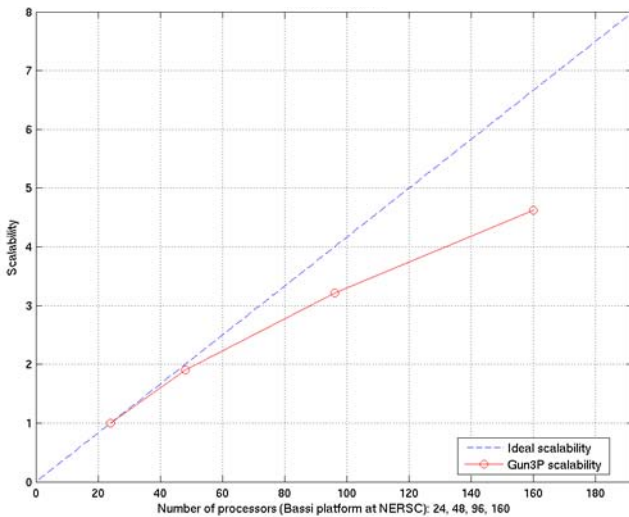


Fig. 12. Gun3P scalability, as of December of 2007.

- [33] S. Humphries and J. Petillo, “Self-magnetic field calculations in ray-tracing codes,” *Laser and Particle Beams*, vol. 18, pp. 601–610, 2000.
- [34] H. Igarashi, “On the property of the curl-curl matrix in finite Element analysis with Edge Elements,” *IEEE Trans. Magn.*, vol. 37, no. 5, pp. 3129–3132, 2001.

## APPENDIX

In the Appendix we focus on the numerical aspects of Gun3P algorithm. A DC gun will be represented by a bounded piecewise-smooth domain  $\Omega \subset \mathbb{R}^3$  with boundary

$$\Gamma = \Gamma_0 \cup \Gamma_{focus} \cup \Gamma_{anode} \cup \Gamma_{out} \cup \Gamma_{gap} \cup \Gamma_{sym},$$

where  $\Gamma_0$  is the grounded electrode which contains the region  $\Gamma_{emi} \subset \Gamma_0$  that emits particles of rest mass  $m_0$  and charge  $e$ ,  $\Gamma_{focus}$  is the focus electrode maintained at a given negative voltage  $V_{focus} < 0$ ,  $\Gamma_{anode}$  is the electrode maintained at a given positive voltage  $V_{anode} > 0$ ,  $\Gamma_{out}$  is the aimed exit region for the particles,  $\Gamma_{gap}$  represents the gap(s) between electrodes and  $\Gamma_{sym}$  represents the symmetry plane(s), if any.

Let  $\hat{\mathbf{n}}$  denote the outward unit normal along  $\Gamma$ . Gun3P then deals with three physical problems:

$$\begin{cases} \nabla \cdot (\epsilon \mathbf{E}) = \rho & \text{in } \Omega, \\ \mathbf{E} \times \hat{\mathbf{n}} = \mathbf{0} & \text{on } \Gamma_0 \cup \Gamma_{focus} \cup \Gamma_{anode}, \\ \mathbf{E} \cdot \hat{\mathbf{n}} = 0 & \text{on } \Gamma_{out} \cup \Gamma_{gap} \cup \Gamma_{sym}, \end{cases} \quad (6)$$

$$\begin{cases} \nabla \times (\mu^{-1} \mathbf{B}) = \mathbf{J} & \text{in } \Omega, \\ \mathbf{B} \cdot \hat{\mathbf{n}} = 0 & \text{on } \Gamma \setminus \Gamma_{sym}, \\ \mathbf{B} \times \hat{\mathbf{n}} = \mathbf{0} & \text{on } \Gamma_{sym}, \end{cases} \quad (7)$$

and

$$\begin{cases} m_0 \frac{d(\gamma \mathbf{v})}{dt} = q[\mathbf{E} + \mathbf{v} \times (\mathbf{B} + \mathbf{B}_{ext})] & \text{for } t > 0, \\ \mathbf{x} = \mathbf{x}_0 & \text{at } t = 0, \\ \mathbf{v} = \mathbf{v}_0 & \text{at } t = 0, \end{cases} \quad (8)$$

where  $\epsilon$  is the permittivity,  $\mu$  is the permeability,  $\gamma$  is the relativistic mass factor,  $\mathbf{x}$  is a particle position,  $\mathbf{v}$  is a particle velocity,  $\mathbf{B}_{ext}$  is an external focusing magnetostatic flux density and  $\mathbf{x}_0 \in \Gamma_{emi}$  and  $\mathbf{v}_0$  are given initial position and velocity of a particle. Above, (6) is the electrostatic problem, (7) is the magnetostatic problem, and (8) is the description of particle trajectories through the relativistic Lorentz equation. It should be pointed out that the boundary condition on  $\Gamma \setminus \Gamma_{sym}$  in (7) is exact for the case of cylindrical symmetric domains and, if such a symmetry is not present, it is still considered to be a good approximation for the case of short pulse DC guns [6], such as the LSBK gun discussed in Section III.

We assume homogeneous isotropic media and express

$$\mathbf{E} = -\nabla \phi \quad \text{and} \quad \mathbf{B} = \nabla \times \mathbf{A}.$$

The tangential continuity of the vector potential  $\mathbf{A}$  guarantees the continuity of the normal component of  $\mathbf{B}$  [17].

### A. Strong Formulations

The strong formulation of the electrostatic problem reads

$$\begin{cases} -\nabla \cdot (\nabla \phi) = \frac{\rho}{\epsilon} & \text{in } \Omega, \\ \phi = 0 & \text{on } \Gamma_0, \\ \phi = V_{focus} & \text{on } \Gamma_{focus}, \\ \phi = V_{anode} & \text{on } \Gamma_{anode}, \\ \frac{\partial \phi}{\partial \hat{\mathbf{n}}} = 0 & \text{on } \Gamma_{out} \cup \Gamma_{gap} \cup \Gamma_{sym}, \end{cases} \quad (9)$$

and the strong formulation of the magnetostatic problem reads

$$\begin{cases} \nabla \times \nabla \times \mathbf{A} = \mu \mathbf{J} & \text{in } \Omega, \\ (\nabla \times \mathbf{A}) \cdot \hat{\mathbf{n}} = 0 & \text{on } \Gamma \setminus \Gamma_{sym}, \\ (\nabla \times \mathbf{A}) \times \hat{\mathbf{n}} = \mathbf{0} & \text{on } \Gamma_{sym}. \end{cases} \quad (10)$$

### B. Weak Formulations

Let  $V_E$  indicate the set of sufficiently smooth scalar test functions  $\varphi : \Omega \rightarrow \mathbb{R}$  satisfying

$$\varphi = 0 \text{ on } \Gamma_0.$$

The weak solution of problem (9) shall then satisfy

$$\begin{aligned} \int_{\Omega} \nabla \phi \cdot \nabla \varphi \, d\Omega &= \int_{\Gamma} \frac{\partial \phi}{\partial \hat{\mathbf{n}}} \varphi \, d\Gamma + \\ &+ \int_{\Omega} \frac{\rho}{\epsilon} \varphi \, d\Omega \quad \forall \varphi \in V_E, \end{aligned} \quad (11)$$

where we have used the identity

$$\begin{aligned} - \int_{\Omega} \Delta \phi \, \varphi \, d\Omega &= \int_{\Omega} \nabla \phi \cdot \nabla \varphi \, d\Omega + \\ &- \int_{\Gamma} \frac{\partial \phi}{\partial \hat{\mathbf{n}}} \varphi \, d\Gamma. \end{aligned}$$

The homogeneous Neumann boundary condition in (9) makes the boundary integral in (11) vanish.

Similarly, let  $V_B$  indicate the set of sufficiently smooth vector test functions  $\mathbf{N} : \Omega \rightarrow \mathbb{R}^3$  satisfying

$$\mathbf{N} \times \hat{\mathbf{n}} \times \hat{\mathbf{n}} = \mathbf{0} \text{ on } \Gamma \setminus \Gamma_{sym}, \quad (12)$$

that is, vector functions that have null tangential component at the boundary. The reason for such condition will become clear in Subsection C. The weak solution of problem (10) shall then satisfy

$$\begin{aligned} \int_{\Omega} \nabla \times \mathbf{A} \cdot \nabla \times \mathbf{N} \, d\Omega &= - \int_{\Gamma} (\hat{\mathbf{n}} \times \nabla \times \mathbf{A}) \cdot \mathbf{N} \, d\Gamma + \\ &+ \int_{\Omega} \mu \mathbf{J} \cdot \mathbf{N} \, d\Omega \quad \forall \mathbf{N} \in V_B \end{aligned} \quad (13)$$

where we have used the identities

$$\begin{aligned} \int_{\Omega} \nabla \times \nabla \times \mathbf{A} \cdot \mathbf{N} \, d\Omega &= \int_{\Omega} \nabla \times \mathbf{A} \cdot \nabla \times \mathbf{N} \, d\Omega + \\ &+ \int_{\Gamma} (\mathbf{N} \times \hat{\mathbf{n}}) \cdot \nabla \times \mathbf{A} \, d\Gamma \end{aligned}$$

and

$$(\mathbf{N} \times \hat{\mathbf{n}}) \cdot \nabla \times \mathbf{A} = (\hat{\mathbf{n}} \times \nabla \times \mathbf{A}) \cdot \mathbf{N}.$$

The boundary condition on  $\Gamma_{sym}$  in (10) makes the boundary integral in (13) vanish.

### C. Discretizations

We discretize both problems with the finite element method [18], generating a tetrahedral mesh  $\Omega_h$  of characteristic size  $h > 0$ . The electrostatic problem uses scalar basis functions [19] and the magnetostatic problem uses hierarchical vector basis functions [24] [22] [20] [23] [21] [25].

Let  $N_E$  denote the number of scalar global basis functions belonging to  $V_E$  and, for  $i = 1, 2, \dots, N_E$ , let  $\varphi_i : \Omega \rightarrow \mathbb{R}$

denote the  $i$ -th global scalar basis function. We then substitute the approximation

$$\phi = \sum_{i=1}^{N_E} \Phi_i \varphi_i$$

into (11) and, after using the basis functions as test functions and correctly imposing the boundary conditions for  $\phi$ , end up with the system of  $N_E$  linear equations

$$\mathbf{M}_E \Phi = \mathbf{b}_{E,Dir} + \mathbf{b}_{E,\rho}, \quad (14)$$

where  $\mathbf{M}_E$  is a  $N_E \times N_E$  matrix,  $\Phi$  is the vector of unknowns  $\Phi_i$ ,  $i = 1, 2, \dots, N_E$ ,  $\mathbf{b}_{E,Dir}$  is the portion of the right hand side (rhs) related to the nonhomogeneous Dirichlet boundary conditions involving potentials  $V_{focus}$  and  $V_{anode}$ , and  $\mathbf{b}_{E,\rho}$  is the portion of the rhs related to the charge generated by the particle trajectories.

Similarly, let  $\tilde{N}_B$  denote the number of vector global basis functions belonging to  $V_B$  and, for  $i = 1, 2, \dots, \tilde{N}_B$ , let  $\mathbf{N}_i : \Omega \rightarrow \mathbb{R}^3$  denote the  $i$ -th global vector basis function. The need for the tilde in  $\tilde{N}_B$  and other symbols will be understood shortly and we shall denote by *edge basis functions* those hierarchical vector basis functions of lowest possible order. If the approximation

$$\mathbf{A} = \sum_{i=1}^{\tilde{N}_B} \tilde{a}_i \mathbf{N}_i$$

is substituted into (13) and basis functions are used as test functions, one obtains a singular  $\tilde{N}_B \times \tilde{N}_B$  matrix  $\tilde{\mathbf{M}}_B$  with

$$\tilde{\mathbf{M}}_{B,i,j} = \int_{\Omega} \nabla \times \mathbf{N}_i \cdot \nabla \times \mathbf{N}_j \, d\Omega, \quad 1 \leq i, j \leq \tilde{N}_B.$$

Besides, it not obvious how to correctly treat the boundary condition on  $\Gamma \setminus \Gamma_{sym}$ . These difficulties are handled in two steps. First, from the theory of hierarchical vector basis functions [21] we know that, for  $p > 1$ , the space spanned by the hierarchical vector basis functions of order  $p$  has either (a) all its basis functions equal to the gradient of scalar functions or (b) all its elements with nonzero curl. For the former case (a), the curl of the basis functions obviously vanish and so we eliminate the degrees of freedom (dof) associated to them. Second, regarding the edge basis functions of lowest order  $p = 1$ , we use the tree-cotree approach [28] [29] [26] [27], that is, once an overall tree has been constructed over  $\Omega_h$  (by ‘‘walking’’ through all its nodes passing only once at any node), we eliminate the basis functions associated to the edges in it, further reducing the order of the problem matrix to a value denoted by  $N_B$  and turning such matrix into a nonsingular one. The cotree is the tree formed by the remainder edges, whose dof continue to exist. A key feature in the tree-cotree approach for the magnetostatic problem is to form the overall tree through three substeps. First, a tree is generated only for the boundary nodes of  $\Omega_h$ . Second, a tree is generated only for the interior nodes of  $\Omega_h$ . Finally, an edge linking both trees is selected. The first substep is necessary for the correct imposition of the boundary condition on  $\Gamma \setminus \Gamma_{sym}$  in (10). Indeed, taking  $\Gamma_2$  to be any closed polygon formed by

boundary edges on  $\Gamma \setminus \Gamma_{sym}$ , the Stokes theorem gives

$$\oint_{\partial\Gamma_2} \mathbf{A} \cdot d\mathbf{l} = \int_{\Gamma_2} \nabla \times \mathbf{A} \cdot \hat{\mathbf{n}} \, d\Gamma = 0.$$

Then, since a graph is a tree if and only if it has no cycles but the addition of any edge results into a unique cycle, we conclude that the dof associated to the unique cotree edge in any such  $\Gamma_2$  will have to value zero as well, that is, the boundary condition on  $\Gamma \setminus \Gamma_{sym}$  becomes the *homogeneous Dirichlet boundary condition*

$$\int_{\ell} \mathbf{A} \cdot d\mathbf{l} = 0 \quad \text{for any mesh edge } \ell \text{ on } \Gamma \setminus \Gamma_{sym}. \quad (15)$$

This concludes the explanation for condition (12). Some references on the numerical solution of the magnetostatic problem are [30] [31] [32] [33] [34].

After dof elimination we then substitute the approximation

$$\mathbf{A} = \sum_{i=1}^{N_B} a_i \mathbf{N}_i$$

into (13), use the basis functions as test functions and impose boundary conditions for  $\mathbf{A}$ , ending up with the system of  $N_B$  linear equations

$$\mathbf{M}_B \mathbf{a} = \mathbf{b}_B, \quad (16)$$

where  $\mathbf{M}_B$  is a  $N_B \times N_B$  matrix and  $\mathbf{a}$  is the vector of unknowns  $a_i$ ,  $i = 1, 2, \dots, N_B$ .

#### D. Particle Tracking

Given a tetrahedral mesh, all cathode triangles are further subdivided into  $n^2$  smaller triangles, as determined by a integer user-defined input parameter  $n$ . Let  $N$  denote the total number of resulting triangles,  $p$  be the subindex used for their designation,  $1 \leq p \leq N$ , and  $\Delta_p$  be the area of a smaller triangle. We also refer to “ $p$ ” as particle id or ray id.

Gun3P sets an emission position  $\mathbf{x}_{0,p}$  at the center of each smaller triangle. As explained in Section II, emission positions are selected during initialization and do not vary from cycle to cycle. Once particles are emitted, Gun3P associates to each emitted particle a ray with current density  $J_{cathode}$  (see equation (3)), current  $I_p = J_{cathode} \cdot \Delta_p$  and infinitesimal cross area  $\delta A_p$ . As the rays travel, their currents are kept constant and their current densities  $J_p$  and cross areas  $\delta A_p$  satisfy

$$J_p \cdot \delta A_p = I_p.$$

A ray path consists of a sequence of connected straight segments, each segment corresponding to a time step in the Boris algorithm [14] used for the discretization of (8). An important tracking task is to provide these segments for the computation of the integrals

$$\int_{\Omega_e} \frac{\rho}{\epsilon} \varphi \, d\Omega_e \quad \text{and} \quad \int_{\Omega_e} \mu \mathbf{J} \cdot \mathbf{N} \, d\Omega_e$$

in any given tetrahedron  $\Omega_e$ . Such integrals are related to the rhs of equations (14) and (16). For the case of an infinitesimal cylinder  $\delta V$  of ray cross area  $\delta A_p$  and length  $\delta l$ , which is

traveled in  $\delta t_p$  time by a ray with velocity  $v_p = \delta l / \delta t_p$ , it is easy to check that

$$\int_{\delta V} \frac{\rho}{\epsilon} \varphi \, d\delta V = \frac{J_p \delta A_p \delta t_p}{\delta A_p \delta l} \varphi \, \delta A_p \delta l = \frac{I_p}{\epsilon v_p} \varphi \, \delta l$$

and

$$\int_{\delta V} \mu \mathbf{J} \cdot \mathbf{N} \, d\delta V = \mu \mathbf{J}_p \cdot \mathbf{N} \, \delta A_p \delta l = \mu \mathbf{I}_p \cdot \mathbf{N} \, \delta l.$$

Let  $N_e$  denote the number of ray segments inside element  $\Omega_e$ ,  $s$  be the subindex used for their designation,  $1 \leq s \leq N_e$ ,  $p_s$  be the id of the ray related to the  $s$ -th segment inside  $\Omega_e$  and  $l_s$  be the length of such segment. We then have

$$\int_{\Omega_e} \frac{\rho}{\epsilon} \varphi \, d\Omega_e = \sum_{s=1}^{N_e} \int_{l_s} \frac{I_{p_s}}{\epsilon v_{p_s}} \varphi \, dl$$

and

$$\int_{\Omega_e} \mu \mathbf{J} \cdot \mathbf{N} \, d\Omega_e = \sum_{s=1}^{N_e} \int_{l_s} \mu \mathbf{I}_{p_s} \cdot \mathbf{N} \, dl,$$

where the velocity  $v_{p_s}$  and both basis functions  $\varphi$  and  $\mathbf{N}$  can vary along  $l_s$ .

#### E. Computation of Densities at Cross Sections

Without loss of generality, let us assume that the the cross section is perpendicular to the  $z$  axis and that it is located at  $z = z_c$ . Gun3P computes the charge density  $\rho_{z=z_c}$  and current density  $J_{z=z_c}$  at a cross section by sampling, as follows. Given an infinitesimal length  $\delta z$ , a sampling cross region (e.g. a rectangle) of area  $S$  and a volume formed by the extrusion of  $S$  from  $z_c - \delta z/2$  to  $z_c + \delta z/2$ , let  $N_c$  be the number of rays crossing  $S$ ,  $r$  be the subindex used for their designation,  $1 \leq r \leq N_c$ ,  $p_r$  be the id of the ray related to the  $r$ -th crossing,  $\delta A_{p_r}$  be its infinitesimal cross section,  $\delta t_{p_r}$  be the time it takes for traveling from  $z_c - \delta z/2$  to  $z_c + \delta z/2$  and  $v_{p_r,z}$  be the  $z$  component of the crossing velocity. One then has:

$$\rho_{z=z_c} = \frac{\sum_{r=1}^{N_c} J_{p_r} \delta A_{p_r} \delta t_{p_r}}{S \delta z} = \sum_{r=1}^{N_c} \frac{I_{p_r}}{S v_{p_r,z}}$$

and

$$J_{z=z_c} = \frac{\sum_{r=1}^{N_c} J_{p_r} \delta A_{p_r}}{S} = \sum_{r=1}^{N_c} \frac{I_{p_r}}{S}.$$

Both densities vary with the sampling region location and size.

#### F. Inter-Cycle Averaging Factor

Gun3P updates  $\rho$  and  $\mathbf{J}$  through cycles with a user-defined inter-cycle averaging factor  $\xi$ ,  $0 < \xi < 1$  [7]. A weight of  $\xi$  is given to the density values obtained with the trajectories most recently computed, while a weight of  $1 - \xi$  is given to the previously used densities. More specifically, let  $\mathbf{b}_{E,\rho}^{(k)}$  and  $\mathbf{b}_B^{(k)}$  indicate the values used in equations (14) and (16) during the  $k$ -th cycle,  $k = 0, 1, \dots, k_{max}$ , and let  $\mathbf{b}_{E,\rho}^{(k+1/2)}$  and  $\mathbf{b}_B^{(k+1/2)}$  indicate the values obtained with the trajectories computed at the end of the same  $k$ -th cycle. Gun3P then sets

$$\mathbf{b}_{E,\rho}^{(0)} = \mathbf{0} \quad \text{and} \quad \mathbf{b}_B^{(0)} = \mathbf{0},$$

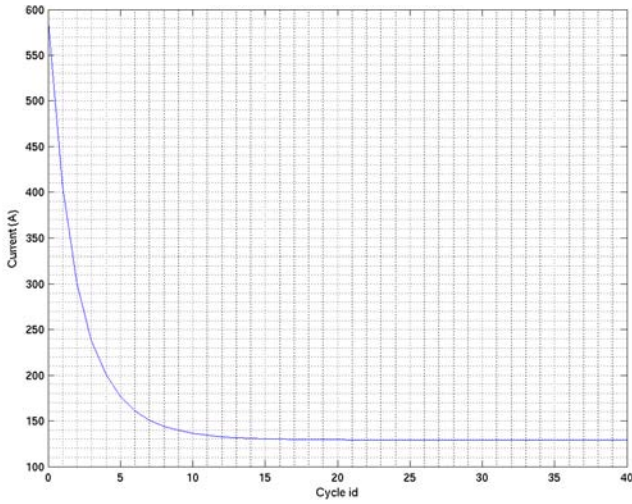


Fig. 13. Gun current convergence, as cycles progress.

$$\mathbf{b}_{E,\rho}^{(k+1)} = \xi \mathbf{b}_{E,\rho}^{(k+1/2)} + (1 - \xi) \mathbf{b}_{E,\rho}^{(k)} \quad \text{for } k \geq 0$$

and

$$\mathbf{b}_B^{(k+1)} = \xi \mathbf{b}_B^{(k+1/2)} + (1 - \xi) \mathbf{b}_B^{(k)} \quad \text{for } k \geq 0.$$

The  $\xi$  parameter plays an important role in the stability of the whole numerical algorithm. Values close to 1 might produce gun current values that overshoot on the first cycle and oscillate on the next cycles, delaying the achievement of the equilibrium value or even causing the overall numerical algorithm to diverge. Proper  $\xi$  values cause these oscillations to be smoothed or even disappear, as shown in Figure 13. For the LSBK DC gun simulation we used  $\xi = 0.1$ .

### G. Cycle Convergence Studies

As stated in Section II, one expects all computed values to stabilize as algorithm cycles progress, and in fact this is the behavior we have been observing on Gun3P simulations. We show some cycle convergence histories in Figures 13, 14 and 15, which are respectively related to the gun current, static fields and crossing positions on the cross plane at  $z = 14\text{cm}$ .

In Figure 13, after 41 cycles, the current changes by about just 4mA around a value of approximately 129A, which represents 0.003%. Figures 14 and 15 also show a persistent decrease of monitored values as cycles advance.

Figure 16 shows that no particles hit the anode on all cycles  $k \geq 22$ , a stable behavior consistent with the convergences observed in the previous three figures.

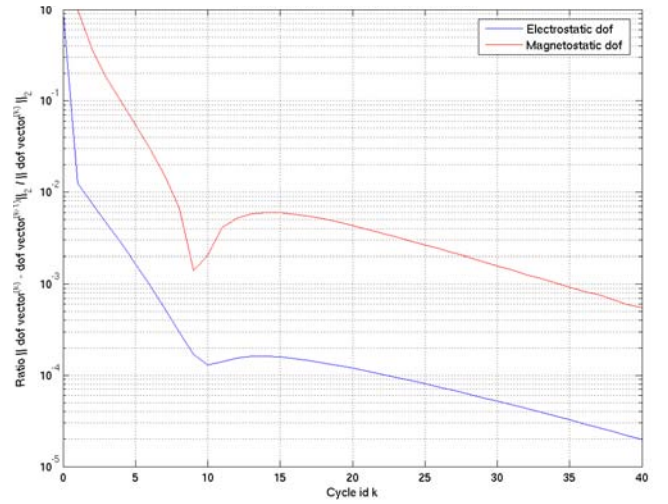


Fig. 14. Relative change of computed dof, as cycles progress.

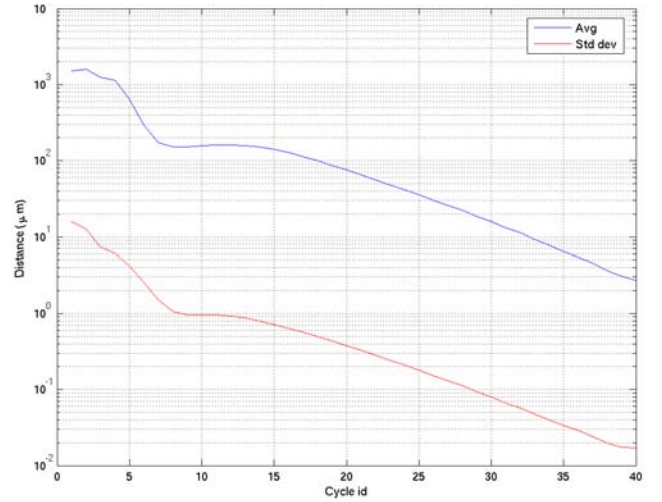


Fig. 15. Distribution of distances ( $\mu\text{m}$ ) of crossing positions on cross plane at  $z = 14\text{cm}$ , between two consecutive cycles, as cycles progress. Each particle has its crossing position in current cycle compared to its crossing position in previous cycle. Only particles crossing on both cycles contribute to the average and standard deviation calculations.

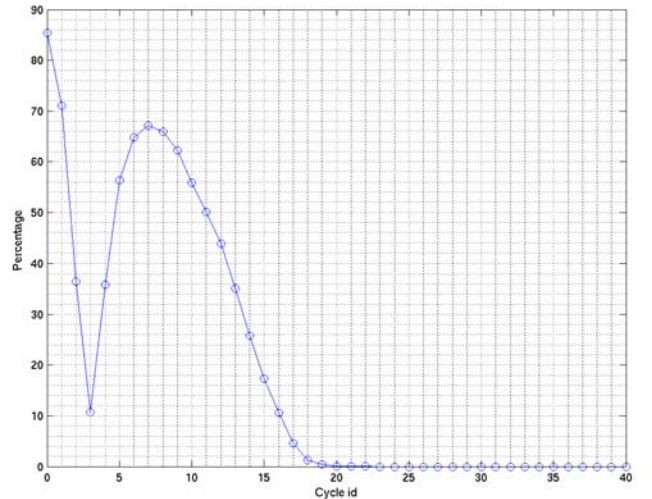


Fig. 16. Percentage of particles hitting the anode, as cycles progress.